Dynamics of cavityless lasing generated by ultrafast multiphoton excitation

Victor Kimberg, Sergey Polyutov, Faris Gel'mukhanov, and Hans Ågren
Department of Theoretical Chemistry, Roslagstullsbacken 15, Royal Institute of Technology, S-106 91 Stockholm, Sweden

Alexander Baev, Qingdong Zheng, and Guang S. He
Institute for Lasers, Photonics and Biophotonics, The State University of New York at Buffalo, Buffalo, New York 14260-3000, USA
(Received 28 April 2006; published 20 September 2006)

A dynamical theory is developed with the purpose of explaining recent experimental results on multiphoton-excited amplified stimulated emission (ASE). Several conspicuous features of this experiment are analyzed, like the threshold dependence of the spectral profile on the pump intensity, and spectral shifts of the ASE pulses co- and counterpropagating relative to the pump pulse. Two models are proposed and evaluated, one based on the isolated molecule and another which involves solvent interaction. The spectral shift between the forward and backward ASE pulses arises in the first model through the competition between the ASE transitions from the pumped vibrational levels and from the bottom of the excited-state well, while in the solvent-related model the dynamical solute-solvent interaction leads to a relaxed excited state, producing an additional ASE channel. In the latter model the additional redshifted ASE channel makes the dynamics of ASE essentially different from that in the molecular model because the formation of the relaxed state takes a longer time. The variation of the pump intensity influences strongly the relative intensities of the different ASE channels and, hence, the spectral shape of ASE in both models. The regime of ASE changes character when the pump intensity crosses a threshold value. Such a phase transition occurs when the ASE rate approaches the rate of vibrational relaxation or the rate of solute-solvent relaxation in the first excited state.

DOI: 10.1103/PhysRevA.74.033814 PACS number(s): 42.65.Re, 42.65.Ky, 42.65.Sf

I. INTRODUCTION

Multiphoton-pumped frequency-up-converted lasing has become one of the most active topics in nonlinear optics and quantum electronics since two-photon-pumped stimulated emission in dye solutions and dye-doped polymer matrices was first observed in the mid-1990s [1–9]. Much of this interest is owing to the fact that many important applications of the effect can be found in the emerging areas of biophotonics and optical communications [10,17], but interest also arises from the fact that the effect is associated with rich interpretations and issues of fundamental physics. Not long ago, three- and four-photon-pumped amplified spontaneous emission (ASE) in solutions was experimentally observed and analyzed theoretically [10–13]. In the case of three-photon [10,13,14] and four-photon [13,15,16] ASE, the pump mechanism requires ultrashort laser pulse sources to provide high peak power [15]. These recent experimental studies of stilbazolium dye solution [13] showed an unusually strong dependence of the ASE spectral profile on pump intensity: the peak position of forward ASE almost coincides with the maximum of steady-state fluorescence for low pump levels, while it experiences a blueshift (20–30 nm) relative to the fluorescence as well as relative to the backward ASE when the pump exceeds certain energy threshold.

To explain this apparently new and surprisingly strong dependence of the ASE spectral profile on the pump intensity, we have developed in the present paper a dynamical theory of ASE based on two different models that take account of experimental data, showing that the effect is essentially dynamical and related to the relaxation of excited states. The first model, which we will henceforth call the "molecular model," is based on vibrational relaxation of the excited electronic state. The pump radiation promotes the molecule from the ground to the first excited electronic state and populates a group of vibrational levels in the Franck-Condon region near the vertical transition energy. The radiative decay from these "vertical" levels to the ground electronic state starts immediately and opens up the first ASE channel. At the same time, these pumped vibrational levels relax nonradiatively to the bottom of the excited-state potential due to intramolecular interaction and interaction with the solvent. The radiative decay from the lowest vibrational level of the excited state also leads to ASE. This second ASE channel is delayed and redshifted relative to the first channel. The two ASE channels compete with each other and the appearance of each channel depends on the Franck-Condon factors of the decay transitions as well as on the pump level. When the pump intensity is larger than a certain threshold level, the ASE rate of the first channel exceeds the rate of nonradiative quenching of the pumped vibrational levels and the first ASE channel starts to dominate.

The background of the second so-called solvent model refers to an instantaneous change of the magnitude and/or direction of the permanent dipole moment of the dye molecule upon excitation. The first ASE channel starts from the nonequilibrium state. This state relaxes to a new state with lower energy within tens to a hundred picoseconds due to relaxation of the solvent molecules around the newly formed dipole. The radiative decay from the relaxed state forms the second ASE channel. Similarly to the molecular model, the threshold occurs when the rate of stimulated emission of the first channel approaches the rate of solute-solvent relaxation in the excited state.

We show that both models can explain the current experiments. To select one of the models, further experimental studies are needed. The applicability of the models is sensi-

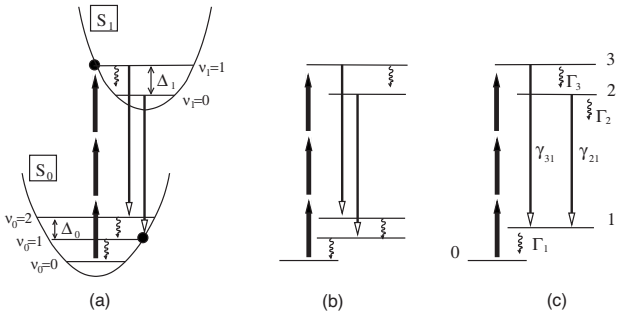

FIG. 1. The molecular model of formation of the ASE spectral profile.

tive to the system and both underlying mechanisms can simultaneously affect the ASE dynamics for some molecules. However, the solvent model is clearly more adequate for experimental situations where the pump pulse is longer than the time of nonradiative depopulation of the pumped level.

The paper is organized as follows. We start in Sec. II from the physical picture of ASE for the molecular and solvent models. The theory of ASE is presented in Sec. III. Results of numerical simulations are analyzed in Sec. IV. Our findings are summarized in Sec. V.

II. PHYSICAL PICTURE

The dynamics of formation of ASE spectral profiles depends on the excited-state vibrational and electronic relaxations. The theoretical considerations coupled to numerical simulations lead to two models that can explain the current experiments. These models—the molecular and solvent models—are described in detail in the following.

A. Molecular model

In the molecular model, we assume that only the lowest vibrational level of the ground electronic state of the molecule with many vibrational modes is initially populated. Figure 1 shows the excitation of the molecule to the first excited electronic state S_1. This excited electronic state can be populated by two-, three-, four-, etc., photon excitations; however, the mechanism of population is not crucial for the physics of ASE formation. Because of this, we discuss here only the case of three-photon population which was studied in the recent experiment reported in Ref. [13]. Figure 1 shows the excitation of a molecule with only one vibrational mode, a simplification that allows the necessary compactness of our explanatory model while still retaining all essential physics.

A strict treatment of the problem studied has to follow the scheme of Fig. 1 with *ab initio* calculations of the multimode Franck-Condon factors. Such an approach was recently developed and implemented for two-photon absorption of polyatomic molecules [18]. At the beginning, only the group of vibrational levels near the point of the vertical transition is populated [level $\nu_1=1$; Fig. 1(a)]. The first ASE channel starts directly from these pumped vibrational levels. These states decay due to the intramolecular vibrational redistribution [19–24] (IVR) and due to the interaction with the solvent [25] (see discussion in Sec. III B). The second, time-delayed, ASE channel is the radiative decay from the bottom of the potential well [level $\nu_1=0$; Fig. 1(a)]. Apparently, this channel selects only the most intensive decay pathway, which is the transition from the bottom of the S_1 well to the point of vertical transition in the ground-state well S_0. We will see below that the pump level strongly influences the relative intensities of these ASE channels when the ASE rate approaches the rate of vibrational relaxation.

The first decay channel from the pumped vibrational level of S_1 (near the point of the vertical transition) deserves a special comment, because a few decay channels can compete with each other. We consider the rather common situation of a moderate displacement of the potential surface under electronic excitation. This allows us to consider only spectral transitions with changes of vibrational quantum numbers $\Delta\nu=0, \pm 1$ [Fig. 1(a)]. We assume also that the vibrational frequency Δ_1 of the excited state S_1 is larger than the vibrational frequency Δ_0 of the ground state. This is in agreement with the experiment [13] which shows smaller broadening of the fluorescence compared to the absorption profile. (However, this is not the only possible explanation of the different bandwidths of the fluorescence and absorption profiles.) Strong self-absorption allows us to neglect the decay channels $S_1\nu_1 \rightarrow S_0\nu_0$ with $\nu_1 \geq \nu_0$ because the transition frequency $\omega(S_1\nu_1 \rightarrow S_0\nu_0)=\omega_0+(\nu_1-\nu_0)\Delta_1+\nu_0(\Delta_1-\Delta_0)$ exceeds the threshold of one-photon absorption $\omega_0=\omega(S_10 \rightarrow S_00)$. However, the photons emitted due to transitions with the change of quantum number by $\nu_0-\nu_1=1$ are not absorbed. Thus, we have two ASE channels $S_11 \rightarrow S_02$ and $S_10 \rightarrow S_01$ with frequencies $\omega(S_11 \rightarrow S_02)=\omega_0+\Delta_1-2\Delta_0$ and $\omega(S_10 \rightarrow S_01)=\omega_0-\Delta_0$, respectively [Fig. 1(b)]. The ASE channel from the pumped vibrational level is blueshifted relative to the ASE channel from the bottom of the potential well: $\Delta\omega=\omega(S_11 \rightarrow S_02)-\omega(S_10 \rightarrow S_11)=\Delta_1-\Delta_0>0$. The peak position of the ASE channel from the bottom of the excited-state well coincides with the maximum of fluorescence. This ASE pulse is delayed relative to the ASE channel from the pumped vibrational level S_11, because the population of the lowest vibrational level takes some time defined by the rate of vibrational relaxation.

Comparison of the widths of fluorescence and one-photon absorption [13] allows one to estimate $\Delta_1-\Delta_0$ and, hence, the spectral shift between the two ASE channels $\Delta\omega$: $\Delta\lambda \sim 10$ nm. The blueshift of the ASE can be explained also by anharmonicity which is larger for the channel $1 \rightarrow 2$ than for $0 \rightarrow 1$. The typical anharmonicity constant (~ 30 cm^{-1}) leads to a 10 nm blueshift. This value is in qualitative agreement with the experimental shift [13] of the forward ASE with respect to the fluorescence (20 nm) measured for high pump levels. We neglect here the direct population of the vibrational state $S_1(\nu_1=0)$ by the pump radiation. This is justified because in the experiment [13] the narrowband pump radiation, with spectral width ~ 10 nm, was tuned almost in resonance with the maximum of photoabsorption [13], $S_0(\nu_0=0) \rightarrow S_1(\nu_1=1)$.

To conclude this section, it looks reasonable to reduce the model depicted in Fig. 1(a) to the scheme shown in Fig. 1(b).

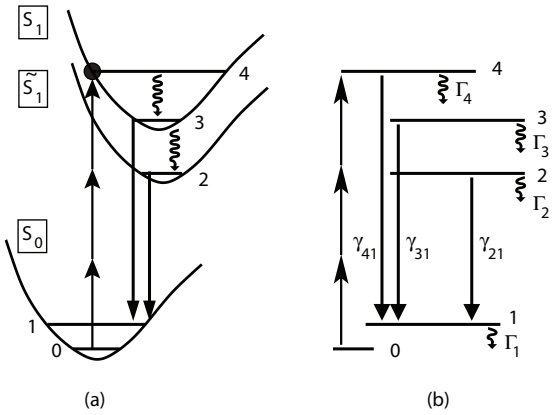

FIG. 2. The solvent model of formation of the ASE spectral profile.

In the numerical simulations we use an energy level scheme that implies the same final state for both ASE channels [Fig. 1(c)]. Such an approximation is justified when the population of the final state by channel $3 \rightarrow 1$ does not influence the ASE channel $2 \rightarrow 1$, and vice versa. This happens if the ASE channel $2 \rightarrow 1$ is delayed relative to the ASE channel $3 \rightarrow 1$ [Fig. 1(c)] with a delay time longer than the lifetime of the final state 1, $\Gamma_1^{-1} \approx 3$ ps (see Sec. IV B).

B. Solvent model

Let us turn our attention to a more general model of ASE, namely, the solvent model [13] (Fig. 2). Similar to the molecular model, the pump radiation promotes the molecules from the lowest vibrational state of the ground electronic state [$S_0|0\rangle$; Fig. 2(a)] to the excited electronic state S_1. Usually, the laser frequency is tuned in resonance with the maximum of photoabsorption, which corresponds to a vertical transition to the vibrational state 4. The pumped vibrational level 4 rapidly relaxes by nonradiative relaxation within ≤ 3 ps to the bottom level 3 of the excited state S_1. The first (fast) ASE channel $3 \rightarrow 1$ occurs due to radiative transition from level 3 to vibrational level 1 of the ground electronic state S_0 [Fig. 2(a)]. The mechanism of formation of the second (slow) ASE channel, following Ref. [13], refers to the polarity of the solvent molecules utilized in the studied cases, in which situation the interaction between the dye molecule and the surrounding solvent molecules is comparatively strong. Upon electronic excitation, the dye molecules instantaneously change the permanent dipole moment $\mathbf{d}_0 \rightarrow \mathbf{d}_e$. The excited state experiences a redshift $\Delta\omega$ due to relaxation of the solvent molecules around the newly formed dipole. This new relaxed state is shown in Fig. 2(a) as $\tilde{S}_1$. This solvent relaxation may occur on a time scale ranging from several tens to a hundred picoseconds, depending on the specific properties of the dye and the solvent [25,26]. After this time interval one can expect to observe the ASE with longer wavelength. In Sec. IV we will discuss these two channels of ASE formation [$3 \rightarrow 1$ and $2 \rightarrow 1$; Fig. 2(b)] taking into account the propagation effects. Simulations (Sec. IV B 2) of the frequency splitting $|\Delta\omega|$ between levels 3 and 2 due to solvation show $\Delta\omega \approx -379.7$ cm^{-1} or $\Delta\lambda \approx 13.5$ nm for the PRL-L3 molecule (Fig. 3) in dimethyl sulfoxide (DMSO) solvent. This value is in good agreement with the experimental value [13] $\Delta\lambda_{\text{expt}} \approx 20$ nm.

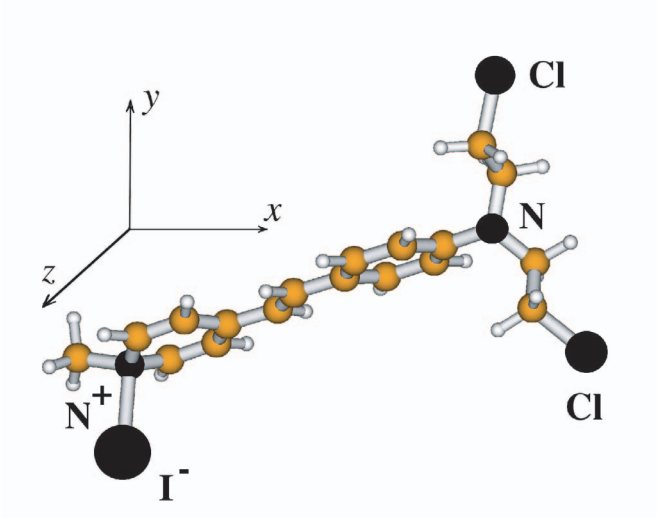

FIG. 3. (Color online) The PRL-L3 molecule.

We will also study the simplified energy level scheme shown in Fig. 2(b). The main objective is to elucidate the role of the pump level in the competition between different ASE channels. It is worthwhile to note that, as in the molecular model, ASE from the pumped level 4 occurs also in the solvent model. The threshold pump level of the $4 \rightarrow 1$ ASE channel is comparable with the threshold of the $3 \rightarrow 1$ channel. So in the general case one can expect three ASE channels in the solvent model: first the $4 \rightarrow 1$ blueshifted ASE pulse appears, followed by the $3 \rightarrow 1$ pulse. The $2 \rightarrow 1$ redshifted ASE pulse experiences the largest delay caused by the solute-solvent relaxation of the excited state. The role of the $4 \rightarrow 1$ channel is diminished when the vibrational relaxation Γ_4 is faster than the duration of the pump pulse. This can occur in the case of a fast ($\lesssim$100–500 fs) IVR depopulation of the pumped level [23].

III. THEORY

In this section we outline the theory of the molecular (Sec. II A) and solvent (Sec. II B) models in accordance with the schemes of transitions depicted in Figs. 1(c) and 2(b), respectively. These simplified schemes select the principal ASE channels.

A. Rate and wave equations

The pump radiation selectively populates a certain excited electron-vibrational state with probability P and initiates the ASE process. In the molecular model [Fig. 1(c)], the ASE dynamics can be described by three rate equations for the populations of levels 3, 2, and 1:

$$\left(\frac{\partial}{\partial t} + \Gamma_3\right)\rho_3 = P - \gamma_{31}(\rho_3 - \rho_1),$$

$$\left(\frac{\partial}{\partial t}+\Gamma_2\right)\rho_2=\Gamma_{32}\rho_3-\gamma_{21}(\rho_2-\rho_1),$$

$$\left(\frac{\partial}{\partial t}+\Gamma_1\right)\rho_1=\Gamma_{31}\rho_3+\Gamma_{21}\rho_2+\gamma_{31}(\rho_3-\rho_1)+\gamma_{21}(\rho_2-\rho_1). \tag{1}$$

The rate equations are slightly different for the four-level solvent model [Fig. 2(b)]:

$$\left(\frac{\partial}{\partial t}+\Gamma_4\right)\rho_4=P-\gamma_{41}(\rho_4-\rho_1),$$

$$\left(\frac{\partial}{\partial t}+\Gamma_3\right)\rho_3=\Gamma_{43}\rho_4-\gamma_{31}(\rho_3-\rho_1),$$

$$\left(\frac{\partial}{\partial t}+\Gamma_2\right)\rho_2=\Gamma_{32}\rho_3+\Gamma_{42}\rho_4-\gamma_{21}(\rho_2-\rho_1),$$

$$\left(\frac{\partial}{\partial t}+\Gamma_1\right)\rho_1=\Gamma_{41}\rho_4+\Gamma_{31}\rho_3+\Gamma_{21}\rho_2+\gamma_{31}(\rho_3-\rho_1)+\gamma_{21}(\rho_2-\rho_1). \tag{2}$$

Here

$$\gamma_{n1}=p_{n1}I_{n1},\quad n=2,3,4, \tag{3}$$

is the rate of ASE transition $n\to 1$ and $I_{n1}=I_{n1}^{+}+I_{n1}^{-}$ is the sum of the intensities of the forward- I_{n1}^{+} and backward- I_{n1}^{-} propagating ASE pulses of the ASE channel $n\to 1$. Γ_i are the rates of depopulation of the levels $i=4$, 3, 2, 1, and Γ_{ij} is the partial decay rate of the nonradiative transition $i\to j$. Generally, the backward-traveling component of the ASE emerging in a real system [10,13] interacts with the forward pulse through the term γ_{n1} in the rate equations. Although the intensity of this component I_{n1}^{-} is usually smaller than that of the copropagating one I_{n1}^{+}, the interaction between the co- and counterpropagating ASE pulses can be important as shown here and earlier [12,27].

We assume that only a small fraction of the molecules is pumped into excited electron vibrational states. Due to this, we also assume that the ground-state population is constant: $\rho_0\approx$const. According to our previous studies [11], this assumption is valid for the pump intensities used in the studied experiment [13]. Both models have two ASE channels. The first channel, $3\to 1$, is fast and starts immediately in the molecular model and with a rather small delay time $\Gamma_{43}^{-1}\approx 3$ ps in the solvent model. The second ASE channel, $2\to 1$, is delayed relative to the first one because the population of the lasing level 2 takes some time to build up (a few Γ_{32}^{-1}). The wave equations for forward- (+) and backward- (−) propagating ASE pulses are the same for both models:

$$\left(\frac{1}{c}\frac{\partial}{\partial t}\pm\frac{\partial}{\partial z}\right)I_{n1}^{\pm}=g_{n1}I_{n1}^{\pm},\quad g_{n1}=B_{n1}(\rho_n-\rho_1)-\alpha,$$

$$n=2,3,4. \tag{4}$$

These equations are written in the slowly varying envelope approximation; we use SI units. The ASE process is initiated by spontaneously generated noise photons with intensity [11] $I(0)\approx 10^{-4}$ W/cm^2. Here,

$$B_{n1}=2\hbar\,\omega_{n1}p_{n1},\quad p_{n1}=\frac{d_{n1}^2}{\Gamma\hbar^2 c\varepsilon_0}. \tag{5}$$

The photoabsorption in the lasing transitions $3\to 1$ and $2\to 1$ is included in the gains g_{n1}. The remaining part of the photoabsorption, α, being weak nonresonant absorption, is neglected in our numerical simulations. Such an approximation breaks down for low pump intensities when $B_{n1}(\rho_n-\rho_1)$ becomes comparable to or smaller than α. However, the result is obvious in this region; indeed, ASE is absent when $g_{n1}\le 0$. The threshold pump intensity $I_p=I_{\text{th}}^{(n)}$ when the ASE starts is defined by the condition

$$g_{n1}(I_{\text{th}}^{(n)})=0. \tag{6}$$

The ASE threshold $I_{\text{th}}^{(n)}$ is different for different ASE channels, due to, for example, different transition dipole moments. The wave equation (4) has a simple, almost strict, solution for the forward ASE:

$$I_{n1}^{+}(t,z)=I(0)\exp\left[\int_0^z g_{n1}\left(t^*+\frac{z_1}{c},z_1\right)dz_1\right] \tag{7}$$

in the characteristic time $t^*=t-z/c=$const, where the gain $g_{n1}(t,z)$ depends on the time t and coordinate z through the rate equations. This solution is not strict due to the backward ASE, the role of which can be important for the solvent model and for the $I_{21}^{+}(t,z)$ component in the molecular model.

All parameters used in the simulations, like the transition dipole moments d_{n1}, resonant frequencies ω_{n1}, homogeneous broadening, Γ, etc., are collected in Tables I and II below and in the figure captions.

B. Role of intramolecular vibrational redistribution

The dynamics of depopulation of the pumped vibrational levels by the redistribution of the excess energy over other vibrational modes is rather complicated. However, experimental data [23,28] shows that the dynamics can be described by a two-exponential model with different time of the pumped level depopulation and time of population of the lowest vibrational level of the active mode. Energy initially localized in one or more Franck-Condon active modes is

TABLE I. The common parameters for the molecular and the solvent models.

L (m)	Γ (eV)	γ (cm^3/GW^2)	N_0 (M)	Γ_1 (s^{-1})	$\Gamma_2=\Gamma_{21}$ (s^{-1})	ω (s^{-1})	ω_{31} (s^{-1})	ω_{21} (s^{-1})	τ (fs)	α (cm^{-1})	w_0 (m^{-2})
10^{-2}	0.1	1.67×10^{-4}	0.02	3×10^{11}	1×10^{9}	1.45×10^{15}	3.25×10^{15}	3.15×10^{15}	100	0	2.39×10^{-9}

TABLE II. Relaxation constants for the molecular and the solvent models in s^{-1} and permanent dipole moments of the PRL-L3 molecule in the ground and the first excited electronic states (in debye).

	Γ_3	Γ_{32}	Γ_{31}	Γ_4	Γ_{43}	$\Gamma_{42}=\Gamma_{41}$
Molecular model	3×10^{11}	2.97×10^{11}	3×10^{9}			
Solvent model	2.15×10^{10}	1.99×10^{10}	1.66×10^{9}	3×10^{11}	2.97×10^{11}	1.5×10^{9}
	$d_0(x)$	$d_0(y)$	$d_0(z)$	$d_e(x)$	$d_e(y)$	$d_e(z)$
	5.3265	4.6241	−4.0414	6.1305	5.4807	−6.7324

rapidly redistributed among a few near-degenerate states because of the anharmonic coupling between modes. These states are in turn each coupled to a successive tier of near-degenerate states via additional low-order resonances $4\rightarrow i\rightarrow j\rightarrow\cdots$. Such a hierarchical coupling scheme of the tier set with increasing density of states results in a sequential energy flow from the active mode [19]. The relevant time scale for departure from the pumped level Γ_4^{-1} (Fig. 4) due to such an intramolecular vibrational redistribution [19–24] was reported to be from below 60 fs to several hundreds of femtoseconds depending on the dye molecule and excitation energy [29–33]. In some cases this process continues up to a few picoseconds (about 6 ps in Ref. [34]). However, the time of arrival Γ_{43}^{-1} at the lowest vibrational level of the active mode due to the energy transfer to nonactive modes is often essentially larger than the time of departure from the pumped level. The reason for this is that among numerous pathways in the entire vibrational space of a molecule only a few end

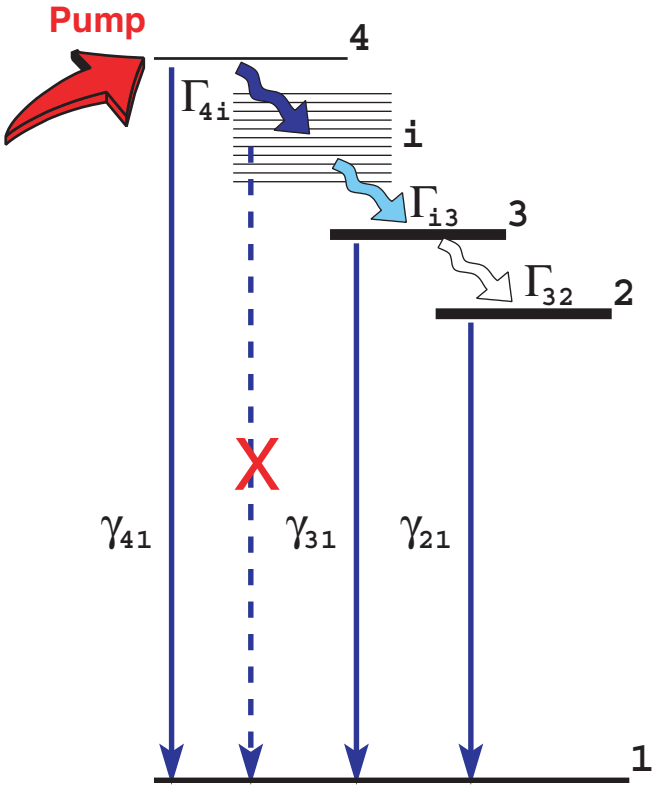

FIG. 4. (Color online) Simplified picture of IVR which takes into account only the active mode (in contrast to the many-mode picture of IVR discussed elsewhere [19,21]).

up in the lowest vibrational state of the active mode, $4\rightarrow i\rightarrow j\rightarrow\cdots\rightarrow 3$ (Fig. 4). It is worthwhile to note that in the general case the lowest state is populated by transitions from different intermediate states i, and the term $\Gamma_{43}\rho_4$ in Eq. (2) should be replaced by $\Sigma_i\Gamma_{i3}\rho_i$. When molecules are dissolved in a solvent, the other mechanism of vibrational cooling of the active mode becomes important. The vibrationally hot molecule equilibrates thermally with the solvent by vibrational energy transfer between low-frequency solute and solvent modes. For many systems vibrational cooling (vibrational relaxation to the lowest vibrational level) was reported to be slower, at least by an order of magnitude, than decay of the pumped level because of IVR [30–33]. By IVR the excess energy is distributed over many intermediate multimode vibrational states with low populations. This amplies a rather weak ASE from these levels except the lowest vibrational level 3 (Fig. 4). Indeed, only this level is finally populated due to the flow of excess energy in the molecular quasicontinuum and in the solvent.

In simulations of the molecular model (Sec. IV A) we ignore the biexponential behavior of the vibrational relaxation and use $\Gamma_3^{-1}\approx\Gamma_{32}^{-1}\approx 3$ ps. Such an approximation is valid for molecules with rather long IVR time (a few picoseconds) [21,34,35]. The fast IVR depopulation of the pumped vibrational level is taken into account in the solvent model (Sec. IV B) by neglecting the ASE channel $4\rightarrow 1$ from the pumped level 4 [see Fig. 2(b)]. This assumption is valid for rather long pump pulses with the duration larger than the IVR time: $\tau_p\Gamma_4\gg 1$.

C. Pumping the upper level by three-photon absorption

As already mentioned, we explore the ASE induced by three-photon absorption, occurring with probability [11]

$$P=\frac{N_0}{\hbar\omega}\sigma^{(3)}I_p^3(t-z/c,z), \tag{8}$$

where N_0 is the concentration of the absorbing molecules in the ground state, and ω is the frequency of the pump field. The cross section of the three-photon absorption is expressed through the three-photon absorption coefficient γ as

$$\sigma^{(3)}=\frac{\gamma}{N_0}. \tag{9}$$

According to Ref. [11] the value of the three-photon absorption coefficient γ for the organic stilbene chromophore

4-[*N*-(2-hydroxyethyl)-*N* (methyl) aminophenyl]-4′-(6-hydroxyhexyl sulfonyl) (abbreviated at APSS) is $\gamma \approx 0.88 \times 10^{-3}$ cm^3/GW^2 (theory) and $\gamma \approx 0.5 \times 10^{-4}$ cm^3/GW^2 (experiment) for $N_0 = 3.6 \times 10^{25}$ m^{-3}. An experimental value of γ for the PRL-L3 dye (Fig. 3) is absent, but the similarity of APSS and PRL-L3 molecules allows us to conclude that the values of the three-photon absorption coefficient are of the same order of magnitude for these molecules. According to experiment [13] we use $N_0 = 1.2 \times 10^{25}$ m^{-3} in our simulations. Because of this we choose $\gamma \approx (0.5/3) \times 10^{-4} = 1.67 \times 10^{-4}$ cm^3/GW^2.

It is reasonable to approximate the shape of the pump pulse by a Gaussian

$$I_p(t - z/c, z) = I_p(r,z) \exp\left[- \left(t - \frac{z - l_0}{c} \right)^2 \frac{\ln 2}{\tau_p^2} \right]. \quad (10)$$

Here, τ_p is the half width at half maximum of the pump pulse, and $z = l_0$ is the peak position of the pump pulse at the moment $t = 0$. We set $l_0 = -4\tau_p c$ in the simulations. The prefactor $I_p(r,z)$ shows the radial distribution of the Gaussian beam along the cell axis z:

$$I_p(r,z) = I_p e^{-\alpha_p (z - l_0)} \left(\frac{w_0}{w(z')} \right)^2 \exp\left(- \frac{2r^2}{w^2(z')} \right),$$

$$w^2(z') = w_0^2 \left[1 + \left(\frac{z' \lambda}{\pi w_0^2} \right)^2 \right] \quad (11)$$

where $z' = z - L/2$, w_0 is the radius of the Gaussian beam waist, while $w(z')$ is the beam waist at distance z' from the focus (center of the cell). The pump intensity is attenuated due to three-photon absorption $\alpha_p = \gamma I_p^2$. In the simulations we approximate the intensity distribution by its distribution on the axis of the beam

$$I_p(r,z) \to I_p(0,z) = I_p \frac{e^{-\alpha_p (z - l_0)}}{1 + \left(\frac{z' \lambda}{\pi w_0^2} \right)^2}. \quad (12)$$

D. Role of the duration and intensity of the pump pulse in formation of ASE

The conventional mechanism of ASE is based on the assumption that ASE is formed only due to the transitions from the bottom of the excited electronic state S_1. However, this is true only for rather long pump pulses $\tau_p \Gamma_3 > 1$. When the pulse is short $\tau_p \Gamma_3 \ll 1$, as in the experiments of Refs. [10,13,17], ASE from upper vibrational levels becomes important. One can see this from the solution of Eqs. (1) for the molecular model [Fig. 1(c)] with a low pump level ($\gamma_{n1} \ll \Gamma_n$)

$$\rho_3(t) = e^{-\Gamma_3 t} \int_0^t P(t_1) e^{\Gamma_3 t_1} dt_1,$$

$$\rho_2(t) = \Gamma_{32} e^{-\Gamma_2 t} \int_0^t \rho_3(t_1) e^{\Gamma_2 t_1} dt_1. \quad (13)$$

The rate of depopulation of 2 is usually small, $\Gamma_2 \ll \Gamma_3$. In the case when the pump pulse is long ($P \approx$ const), mainly the bottom of the S_1 potential is populated due to the effect of optical pumping,

$$\rho_3(t) \approx P \left(\frac{1 - e^{-\Gamma_3 t}}{\Gamma_3} \right), \quad \rho_2(t) \approx \frac{\rho_3^{\max} \Gamma_{32}}{\Gamma_2} (1 - e^{-\Gamma_2 t}) \gg \rho_3^{\max}. \quad (14)$$

Here, $\rho_3^{\max} = P/\Gamma_3$ is the maximal population of the upper level. Thus, ASE occurs only due to radiative transitions from the bottom of the S_1 well and the peak position of the ASE spectrum coincides with the fluorescence maximum. The picture changes qualitatively when the pump pulse is shorter than the lifetime of the upper state 3, $\tau_p \Gamma_3 \ll 1$. Now the populations of both levels can be comparable,

$$\rho_3(t) \approx S(t) e^{-\Gamma_3 t}, \quad \rho_2(t) \approx \frac{\rho_3^{\max} \Gamma_{32} e^{-\Gamma_2 t}}{\Gamma_3} (1 - e^{-\Gamma_3 t}) \lesssim \rho_3^{\max}. \quad (15)$$

Here, $\rho_3^{\max} = S(\infty)$, $S(t) = \int_o^t dt_1 P(t_1)$. Thus, when the pulse is short, ASE, as well as the fluorescence, acquires a double-peak structure due to transitions $3 \to 1$ and $2 \to 1$. This analysis is valid only for small pump intensities, where the relative intensities of the doublet are defined by the square of the ratio of the transition dipole moments, d_{31}^2/d_{21}^2.

The pump intensity is another important parameter that influences the ASE dynamics. Indeed, when the pump level is high, the upper state 3 [Fig. 1(c)] is also depopulated with rate γ_{31} due to stimulated emission, which promotes the excited molecules to the final state 1. Apparently, this ASE channel $3 \to 1$ suppresses the nonradiative population $3 \to 2$ of the lasing level 2. The nonradiative population of level 2 is almost quenched when the ASE channel is faster than the nonradiative quenching of the pumped level $3 \to 2$: $\gamma_{31} \gg \Gamma_3$. In this case, the double-peak ASE spectrum is transformed to a single-peak profile due to the dominant contribution of the blue component $3 \to 1$. When the rate of stimulated emission γ_{31} approaches the rate of nonradiative decay Γ_3, the ASE spectrum changes qualitatively. The threshold pump intensity of this effect, I_0, is defined by the condition

$$\gamma_{31}(I_0) = \Gamma_3. \quad (16)$$

We would like to point out the difference between the threshold I_0 and the threshold of the ASE, $I_{\text{th}}^{(n)}$, defined by Eq. (6). It is also worthwhile to mention that the threshold I_0' of the $4 \to 1$ ASE channel in the solvent model

$$\gamma_{41}(I_0') = \Gamma_4 \quad (17)$$

in general differs from the $3 \to 1$ threshold (16). In the following section we study the dynamics of ASE induced by short pump pulses more precisely using numerical solutions of the coupled rate and wave equations.

IV. NUMERICAL MODELING OF FORWARD AND BACKWARD ASE

We begin this section by analyzing the results of numerical simulations of the three-photon pumped ASE dynamics, experimentally studied recently for stilbazolium dye solutions (PRL-L3 and PRL-L10 molecules) [13]. Parameters that are common for the molecular and solvent models are collected in Table I. Table II includes the relaxation constants, which are different in these two models, and permanent dipole moments of the molecule in the ground and first excited electronic states calculated for the solvent model. The solute-solvent relaxation of the excited-state potential of the solvent model (see Fig. 2) is very sensitive to both solute and solvent, and the corresponding relaxation time Γ_{32}^{-1} varies in a broad region ~100 fs–100 ps [23]. We use $\Gamma_{32}^{-1}=50$ ps.

The theory has been coded exploiting numerical methods for solving the ordinary differential equations (1) and (2) and the partial differential equations (4). The wave equations (4) were solved with the following initial and boundary conditions: $I^{\pm}(0,z)=I^{+}(t,0)=I^{-}(t,L)=I(0)=10^{-4}$ W/cm^2. In accordance with the studied experiment [13], the equations are solved for a cell of length $L=1$ cm.

A. Dynamics of ASE in the molecular model

Let us first discuss the ASE formation in the framework of the molecular model. The results of the numerical simulations of this model are presented in Figs. 5–7, 9, and 10 below. We explore two cases: (A) the transition dipole moments of the ASE transitions $3\rightarrow1$ and $2\rightarrow1$ are the same, and (B) the transition dipole moment of the fast transition $3\rightarrow1$ is smaller than that of the adiabatic transition $2\rightarrow1$. The transition dipole moments differ from each other due to the Franck-Condon amplitudes of these transitions. In our simulation we use $d_{S_1S_0}=9.9$ D and $d_{31}=\langle 3|1\rangle d_{S_1S_0}$, $d_{21}=\langle 2|1\rangle d_{S_1S_0}$. The values of the transition dipole moments d_{31} and d_{21} are given in the figure captions.

Figure 5 shows the branching ratios of two ASE channels, $I_{31}/(I_{31}+I_{21})$, for the peak intensities of forward and backward pulses at the end of and at the entry to the cell, respectively. The branching ratio for the forward ASE changes qualitatively when the pump level crosses the threshold I_0 [see Eq. (16) and Fig. 5]. Such a threshold is not seen for the backward ASE in the studied region of pump intensities. The ratio of the dipole moments of transitions $3\rightarrow1$ and $2\rightarrow1$ influences the value of the threshold pump intensity I_0 as well as the branching ratio below the threshold [compare Figs. 5(a) and 5(b)]. The corresponding spectra of forward and backward ASE are shown in Figs. 6(a) and 6(b). One can see that below the threshold I_0 only case B shows the suppression of the blue peak $3\rightarrow1$ in agreement with the experimental results [13]. However, above the threshold $I_p>I_0$ both cases A and B display the same trend $I_{31}\gg I_{21}$ as the experiment [13].

Let us discuss case B in more detail. When the pump intensity is very small ($\lesssim 0.3I_0$, Fig. 5) the two ASE channels $2\rightarrow1$ and $3\rightarrow1$ have comparable probabilities defined by the square of the transition dipole moment (see Sec. III D). It is necessary to recall that the "pure" gain $B_{n1}(\rho_n-\rho_1)\propto I_p^3$ can

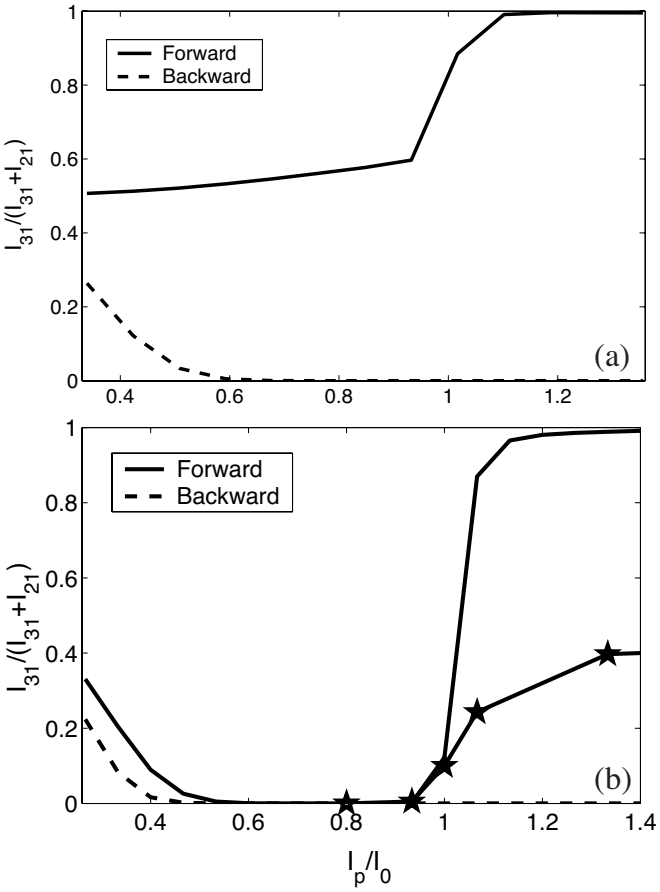

FIG. 5. Branching ratio versus the pump intensity I_p (molecular model). The branching ratios are computed at the entry ($z=0$) and at the end ($z=L$) of the cell for backward and forward ASE, respectively. (a) The same transition dipole moments for ASE transitions: $d_{31}=d_{21}=7.73$ D; $I_0=217$ GW/cm^2. (b) Different transition dipole moments: $d_{31}=5.67$ D, $d_{21}=8.12$ D; $I_0=276$ GW/cm^2. The case $\tau_p\Gamma_{32}>1$ with $\Gamma_{32}^{-1}=50$ fs is shown by pentagrams; $I_0\approx 750$ GW/cm^2 (see the text).

be smaller in this region than the weak nonresonant absorption α [see Eq. (4)]. This means that the ASE is absent for low pump levels and our simulations are valid only above the ASE threshold $I_p>I_{\text{th}}$ [Eq. (6)], because the weak nonresonant absorption α is ignored in the calculations (see Sec. III D). Both forward and backward ASE of the slow $2\rightarrow1$ channel dominates for moderate pump intensities ($0.5<I_p/I_0<1$). When the pump intensity exceeds the threshold I_0 [Eq. (16)], the forward ASE is switched to the fast channel $3\rightarrow1$, while the slow $2\rightarrow1$ channel continues to give the major contribution into the backward ASE up to pump intensities $1.4I_0$ (see Figs. 5 and 6). To understand such a distinction between forward and backward ASE, let us look at the competition of the ASE rates γ_{31} and γ_{21} of these channels with the nonradiative decay rate Γ_{32} (Fig. 7). When the pump level exceeds the threshold I_0 ($\gamma_{31}>\Gamma_{32}$) level 3 decays mainly to level 1. Due to this circumstance, the population of level 2 and, hence, the forward ASE channel $2\rightarrow1$ is suppressed above the threshold I_0 (Fig. 6). The picture is qualitatively different for the backward ASE. The ASE rate at the entry to the cell ($z=0$) originates only from the backward

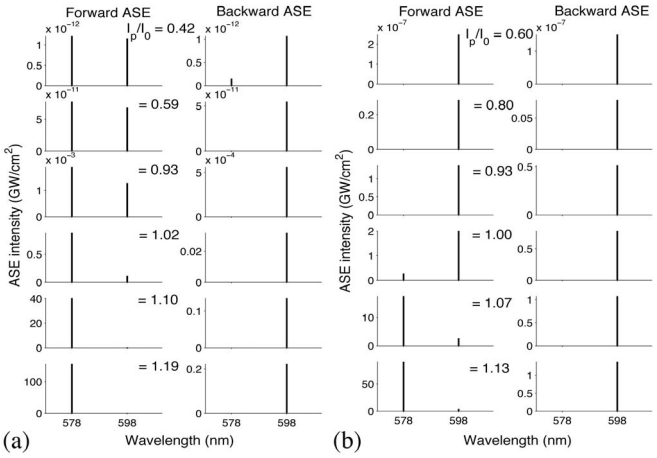

FIG. 6. Spectra of the forward and backward ASE (molecular model). (a) The same transition dipole moments: $d_{31}=d_{21}=7.73$ D; $I_0=217$ GW/cm^2. (b) Different transition dipole moments: $d_{31}=5.67$ D, $d_{21}=8.12$ D; $I_0=276$ GW/cm^2.

ASE, because the forward ASE is absent here. Figure 7 shows that, contrary to the forward ASE, the pump intensity does not reach the threshold value $I_0^{(b)}$ for the backward ASE, because $\gamma_{31}<\Gamma_{32}$ for backward ASE pulses in both cases A and B. Due to this situation, the backward ASE of the channel $3\rightarrow1$ is absent up to the pump intensity $1.4I_0$ (Figs. 5 and 6), and the spectrum of backward ASE consists of only a single resonance $2\rightarrow1$.

Let us now pay attention to the strong dependence of the forward ASE on the transition dipole moments below threshold I_0 [compare Figs. 5(a) and 5(b)]. One can see an almost complete quenching of the forward ASE channel 31 when $d_{21}/d_{31}=1.43$ (case B), contrary to the case with the same transition dipole moments (case A). One can understand this with the help of a solution of (15), which states that the lasing levels 3 and 2 have comparable populations below the threshold I_0. This means that the branching ratio below the

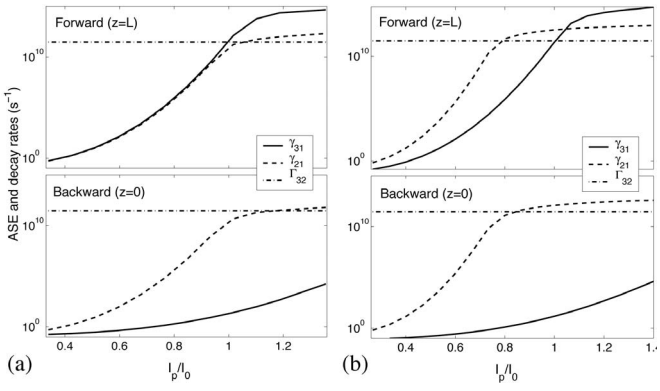

FIG. 7. The ASE rates γ_{31} and γ_{21} as functions of the pump intensity (molecular model). The rates for forward and backward ASE are given at the end ($z=L$) and at the entry ($z=0$) of the cell, respectively. (a) Transition dipole moments of ASE transitions are the same: $d_{31}=d_{21}=7.73$ D; $I_0=217$ GW/cm^2. (b) Transition dipole moments are different: $d_{31}=5.67$ D, $d_{21}=8.12$ D; $I_0=276$ GW/cm^2.

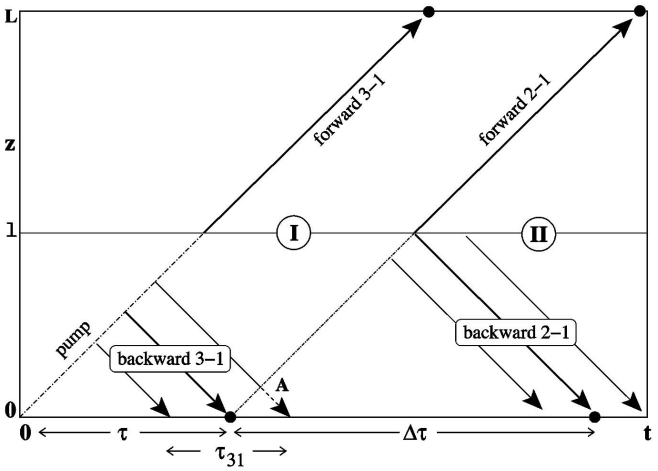

FIG. 8. Scheme of formation of the forward and backward ASE pulses for channels $3\rightarrow1$ and $2\rightarrow1$. The zt plane is divided by convention into the regions I and II where $(g_{31}>0, g_{21}\approx0)$ and $(g_{31}<0, g_{21}>0)$, respectively. The label A marks the absorption region $(g_{31}<0)$ of the backward $3\rightarrow1$ pulse. The forward and backward pulses have large intensities in the regions $z>l$ and $z<l$, respectively.

threshold must be about 0.5 when $d_{21}=d_{31}$ [see Fig. 5(a)]. Apparently, the intensity of the $2\rightarrow1$ channel must be essentially larger than the intensity of the $3\rightarrow1$ channel when $d_{21}>d_{31}$. This explains the suppression of the branching ratio below the threshold in Fig. 5(b). We would like to point out the strong (exponential) dependence of the ASE intensity on the dipole moment (7): $I_{n1}(L)\approx I(0)\exp(g_{n1}L)$, $g_{n1}\propto d_{n1}^2$. For $d_{21}/d_{31}=1.43$ we get $I_{21}(L)/I(0)\approx[I_{31}(L)/I(0)]^2$. This estimation is in good agreement with the strict solution for $I_p/I_0\approx0.8$ $[I_{21}(L)\approx0.01$ GW/cm^2, $I_{31}(L)\approx3\times10^{-8}$ GW/cm^2, $I(0)\approx10^{-13}$ GW/cm$^2]$ which shows strong enhancement of the $2\rightarrow1$ channel due to the larger dipole moment.

1. Duration and delay times of the forward and backward ASE pulses

The forward and backward pulses are formed in qualitatively different ways due to different trajectories of these pulses in the zt plane (Fig. 8). The dynamics of the forward and backward ASE pulses for the pump intensities investigated below, about, and above the threshold intensity I_0 for the cases A ($d_{31}=d_{21}$) and B ($d_{31}<d_{21}$), are shown in Figs. 9 and 10, respectively.

The forward ASE pulse of channel $3\rightarrow1$ appears immediately after the pump pulse and propagates along the same characteristic $z=ct$ as the pump pulse with time of flight $t_{\text{prop}}=L/c=33$ ps. This ASE pulse is shorter than the lifetime of level 3 (≈3 ps) and it experiences narrowing with an increase of the pump level. The reason for this behavior lies in the exponential dependence on the gain (7), $I_{31}^{+}\sim e^{g_{31}L}$. The forward pulse $2\rightarrow1$ is delayed relative to the forward $3\rightarrow1$ pulse because the population of level 2 takes time, $1/\Gamma_{32}\approx3$ ps. However, simulations (Fig. 9) indicate that the delay time is longer than the lifetime of this level, $1/\Gamma_3\approx1/\Gamma_{32}\approx3.4$ ps. Such a delay

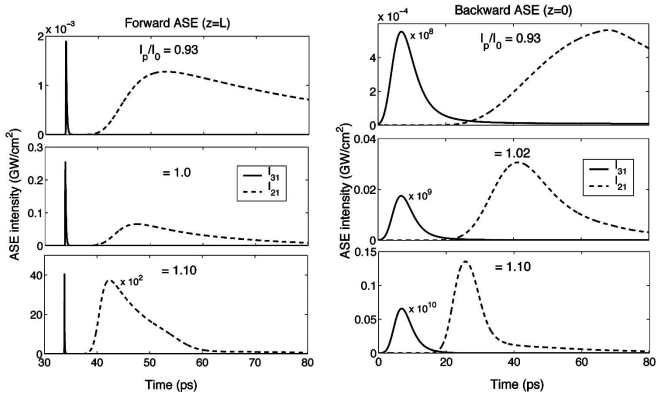

FIG. 9. Time evolution of the forward and backward ASE pulses (molecular model). The forward and backward ASE pulses are shown at the end ($z=L$) and at the entry ($z=0$) of the cell, respectively. The same transition dipole moments: $d_{31}=d_{21}=7.73$ D; $I_0=217$ GW/cm^2.

$$\tau \approx \frac{1}{\Gamma_{32}} \ln \frac{\Gamma_{32}+\Gamma_2}{\Gamma_2} \approx \frac{5.7}{\Gamma_{32}} \approx 19 \text{ ps} \tag{18}$$

follows from the time dependence (15) of the population of level 2, $\rho_2 \propto (1-e^{-\Gamma_{32}t})e^{-\Gamma_2 t}$. When the pump intensity is sufficiently large, the delay τ of the forward pulse $2 \to 1$ becomes shorter (Figs. 9 and 10), because the decay rate Γ_2 of level 2 increases in Eq. (18) due to the ASE rate: $\Gamma_2 \to \Gamma_2 + \gamma_{21}$ (see also below).

The dynamics of the backward pulses differs qualitatively from the forward pulses because of the "orthogonality" of the trajectory in the zt plane (Fig. 8) to the pump propagation. Let us first discuss the $3 \to 1$ backward pulse. The maximum of this pulse reaches the entry of the cell at the instant $\sim\tau$. What strikes the eye here is the large width of this pulse, $\Delta\tau_{31}$, compared to the duration of the forward $3 \to 1$ pulse (see Figs. 9 and 10). This large broadening originates in the geometry of the formation of the backward pulse (Fig. 8), which has nothing to do with the short lifetime of level 3. As

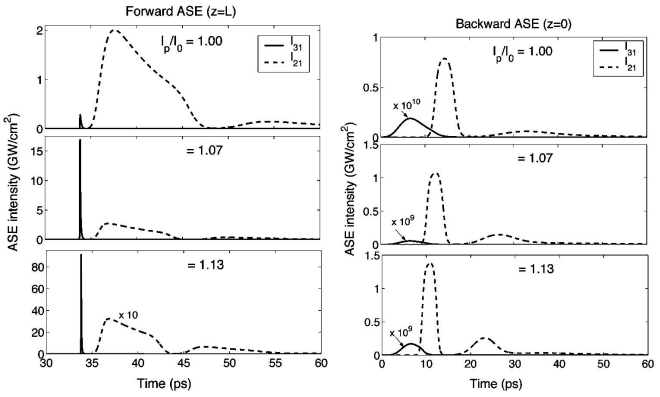

FIG. 10. Time evolution of the forward and backward ASE pulses (molecular model). The forward and backward ASE pulses are shown at the end ($z=L$) and at the entry ($z=0$) of the cell, respectively. Different transition dipole moments: $d_{31}=5.67$ D, $d_{21}=8.12$ D; $I_0=276$ GW/cm^2.

one can see from Fig. 8, both earlier and later (than τ) $3 \to 1$ backward rays reach the entry to the cell. Earlier rays ($t<\tau$) have smaller intensity [$I_{31}^- \sim \exp(g_{31}ct/2)$] than the peak value due to the shorter region of the gain (Fig. 8). It useful to divide the zt plane into regions I and II with large populations of the lasing levels 3 and 2, respectively (Fig. 8). Due to depopulation of level 3 in region II, the gain g_{31} is negative here. The later rays ($t>\tau$) have also smaller intensities, because the $3 \to 1$ radiation is absorbed when it arrives in region II with negative gain $g_{31}<0$ (the absorption region is marked by label A in Fig. 8). Thus, one can conclude that the width of the backward $3 \to 1$ pulse has the order of magnitude $\Delta\tau_{31} \gtrsim 2/cg_{31}$, which is larger than $1/\Gamma_3$.

We pause to mention that forward and backward pulses have large intensities near the end ($z>l$) of and the entry ($z<l$) to the cell, where $z=l$ is the conditional boundary between these pulses (Fig. 8). The order of magnitude of l is $L/2$ for low pump levels and this boundary is shifted to the lower half plane $l \sim L/10$ when the pump approaches the threshold (16) (see Figs. 14 and 16 below). Forward ASE pulses depopulate lasing levels 3 and 2 in the upper half plane ($z>l$) because the forward pulses are strong here. Due to this circumstance, the backward pulses are formed mainly in the lower half plane ($z<l$). The conditionality of such a boundary is obvious; the boundary between the forward and backward pulses is diffuse in reality. The backward and forward pulses interact with each other in the transition region. Such an interaction results in a modulation [27] of the backward and forward $2 \to 1$ pulses (Fig. 10).

Figures 9 and 10 show another effect, the delay between the $2 \to 1$ and $3 \to 1$ pulses longer for backward than for forward propagation, and this delay depends on the pump level. The backward pulse $2 \to 1$ starts to grow when level 2 is populated. Figure 8 shows that this ASE radiation begins to build up from the characteristic of the forward $2 \to 1$ pulse. The intensity of the backward $2 \to 1$ pulse increases with increase of the delay time $\Delta\tau$, because of the increase of the optical path length (Fig. 8). However, the backward $2 \to 1$ optical path length ceases to grow when the $2 \to 1$ ray crosses the boundary $z=l$ (Fig. 8). The crossing point gives the peak position of the $2 \to 1$ pulse and it allows us to estimate the delay time between the backward $2 \to 1$ and $3 \to 1$ pulses: $\Delta\tau \approx 2l/c$. It is worthwhile to note that the intensity of the $2 \to 1$ pulse for longer delay times decreases with the growth of the rate $\Gamma_2+\gamma_{21}$ of depopulation of level 2. We will see below that the ASE quenching of level 2 shortens the delay time $\Delta\tau$, as well as the duration of the $2 \to 1$ pulse.

Let us now discuss the shortening of the pulse duration and the delay times between pulses (Figs. 9 and 10) caused by the increase of the pump intensity. When the pump approaches the threshold, the lifetimes of the lasing levels 3 $[1/(\Gamma_3+\gamma_{31})]$ and 2 $[1/(\Gamma_2+\gamma_{21})]$ become shorter due to an increase of the ASE rates $\gamma_{31}^{\pm}=p_{31}I_{31}^{\pm}$ and $\gamma_{21}^{\pm}=p_{21}I_{21}^{\pm}$. This leads to a narrowing of the ASE pulses in the time domain. Such a shortening of the pulse duration depends strongly on the ASE channel. One can see a moderate narrowing of the $3 \to 1$ component of the forward pulse (see left panels of Figs. 9 and 10); indeed, the lifetime of level 3 decreases approximately two times at the threshold (16): $\Gamma_3^{-1} \to (\Gamma_3$

$+\gamma_{31}^{+})^{-1} \approx (2\Gamma_3)^{-1}$, because here $\gamma_{31}^{+} \approx \Gamma_3$ [see Eq. (16)]. The $3 \rightarrow 1$ component of the backward pulse (right panels of Figs. 9 and 10) almost does not change the width $(\Gamma_3 + \gamma_{31}^{-})^{-1}$, due to the small ASE rate γ_{31}^{-} (see lower panels in Fig. 7). However, both $2 \rightarrow 1$ forward and $2 \rightarrow 1$ backward pulses experience strong narrowing in the time domain $\Gamma_2^{-1} \rightarrow (\Gamma_2 + \gamma_{21}^{\pm})^{-1}$ (Figs. 9 and 10), when the pump level is high enough. This is due to the small value of $\Gamma_2 = 10^9$ s^{-1} compared with the large ASE rates near the threshold $\gamma_{21}^{\pm} \sim \Gamma_3 \approx 3 \times 10^{11}$ s^{-1} (see Fig. 7). An increase of the pump intensity leads also to a decrease of the delay time between $2 \rightarrow 1$ and $3 \rightarrow 1$ (both forward and backward) pulses (Figs. 9 and 10). The reason for this is an enhancement of the depopulation rate of level 2, $\Gamma_2 \rightarrow \Gamma_2 + \gamma_{21}^{\pm}$, and, hence, a shortening of the delay time (18).

As it was mentioned above (Sec. III B), the effective time of depopulation of the pumped vibrational level can be shorter than 3 ps, the value used in the above simulations. Due to this, we also performed calculations with $\Gamma_1^{-1} \approx \Gamma_3^{-1} \approx \Gamma_{32}^{-1} \approx 3$ ps, 200 fs, and 50 fs for a cavity length of $L = 1$ mm. It is worthwhile to note that these calculations do not describe properly the IVR mechanism if $\Gamma_3 \gg \Gamma_{32}$. It turns out that shortening of Γ_{32}^{-1} reduces the delay time τ, in agreement with Eq. (18): $\tau \approx 2.6$ ps, 190 fs, and 50 fs for $\Gamma_{32}^{-1} = 3$ ps, 200 fs, and 50 fs near the threshold pump level. On the other hand, the threshold pump intensity (16) increases when the vibrational relaxation becomes faster. Figure 5(b) shows that the branching ratio of forward ASE is qualitatively different for slow $(\tau_p \Gamma_{32} > 1)$ and fast $(\tau_p \Gamma_{32} < 1)$ vibrational relaxation, in agreement with Eqs. (14) and (15).

B. ASE formation in the solvent model

Following the molecular model we consider the ASE dynamics for two cases: A) $d_{31} = d_{21}$, and B) $d_{31} \neq d_{21}$ also in the solvent model. The ASE channel $4 \rightarrow 1$ is related to the direct transition from the pumped vibrational levels and was studied already in the molecular model above. We ignore this channel in our simulations as the Franck-Condon factor $\langle 4|1\rangle^2$ is assumed small. The maps of ASE pulses in the zt plane (Figs. 14 and 16) show that, contrary to the forward ASE, the backward ASE pulses are localized near the entry to the cell. In general, the mechanism of formation of the ASE pulse and of the spectrum for the solvent model is quite similar to that in the molecular model. One can see this from the dynamics of the branching ratio (Figs. 5 and 11) and the ASE spectra (Figs. 6 and 12), as well as from the dependences of the ASE rates on the pump intensity (Figs. 7 and 13). However, one can see also rather strong distinctions. First of all, the duration of the forward $3 \rightarrow 1$ pulse is much longer (≈ 3 ps) in the solvent model (Figs. 14–16). Contrary to the molecular model, this pulse is now delayed relative to the pump pulse: 11 ps for case A (Figs. 14 and 15), and 7 ps for the case B (Fig. 16). The reason for this second distinction is that the population of the lasing level 3 now takes time $1/\Gamma_{43} \approx 3$ ps, contrary to the molecular model where this level is populated immediately.The mechanism of this delay is similar to the delay of the $2 \rightarrow 1$ pulse in the molecular model [see Eq. (18) and Figs. 9 and 10].

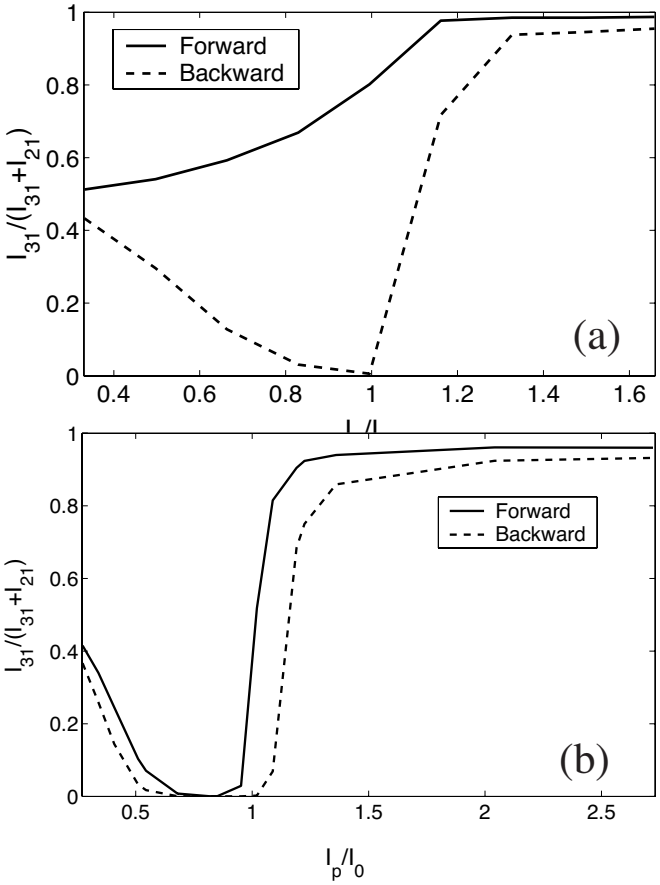

FIG. 11. Branching ratio versus the pump intensity (solvent model). (a) Same transition dipole moments: $d_{31} = d_{21} = 7.73$ D; $I_0 = 222$ GW/cm^2. (b) Different transition dipole moments: $d_{31} = 6.18$ D, $d_{21} = 7.73$ D; $I_0 = 271$ GW/cm^2.

It is worthwhile to point out that an important quantitative distinction of the solvent model is the relaxation time $\Gamma_{32}^{-1} \approx 50$ ps, which is much longer than the relaxation time in the molecular model $\Gamma_{32}^{-1} \approx 3$ ps (Table II). This means that level

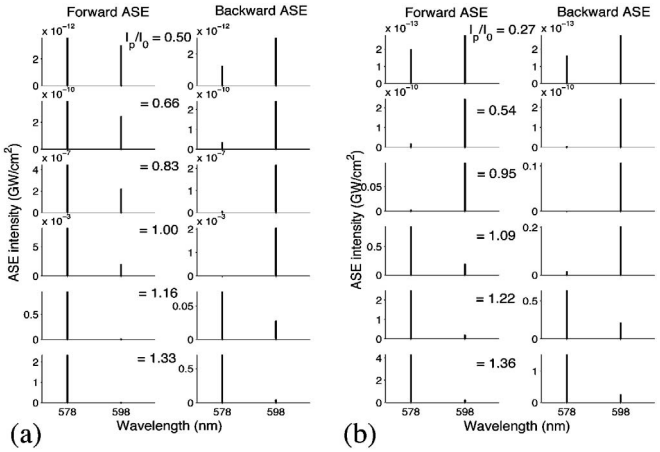

FIG. 12. Spectra of the forward and backward ASE (solvent model). (a) The same transition dipole moments: $d_{31} = d_{21} = 7.73$ D; $I_0 = 222$ GW/cm^2. (b) Different transition dipole moments: $d_{31} = 6.18$ D, $d_{21} = 7.73$ D; $I_0 = 271$ GW/cm^2.

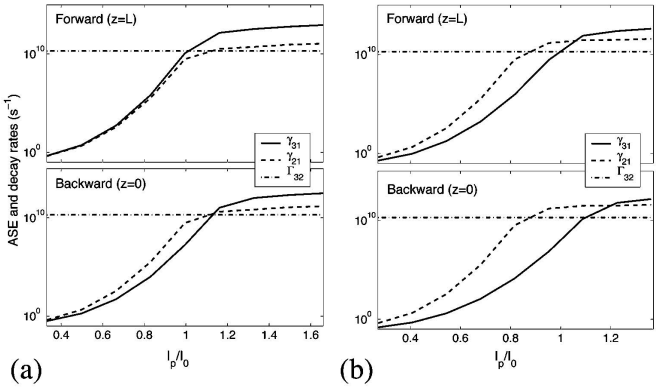

FIG. 13. ASE rates γ_{31} and γ_{21} as functions of the pump intensity I_p (solvent model). (a) Same transition dipole moments: $d_{31}=d_{21}=7.73$ D; $I_0=222$ GW/cm^2. (b) Different transition dipole moments: $d_{31}=6.18$ D, $d_{21}=7.73$ D; $I_0=271$ GW/cm^2.

2 is essentially more slowly populated than in the molecular model, and, hence, this results in a larger delay time (18) between the $2\rightarrow1$ and $3\rightarrow1$ pulses. For example, this delay for the forward pulses is $\approx$146 ps for case A (Fig. 14) and $\approx$50 ps for case B (Fig. 16). Similarly to the molecular model, the delay time depends strongly on the intensity of the pump pulse.

Figure 12 (see also Figs. 11 and 13) displays an interesting effect: The pump intensity changes drastically the spectrum of the backward ASE, in contrast to the single-peak spectrum in the molecular model (Fig. 6). One can see the reason for this from comparison of Figs. 13 and 7: the backward $3\rightarrow1$ ASE rate in the solvent model reaches the threshold $\gamma_{31}=\Gamma_{32}$ with pump intensity close to the threshold of the forward $3\rightarrow1$ channel, I_0. Contrary to the molecular model (Fig. 6), only the blue $3\rightarrow1$ peak forms both forward and

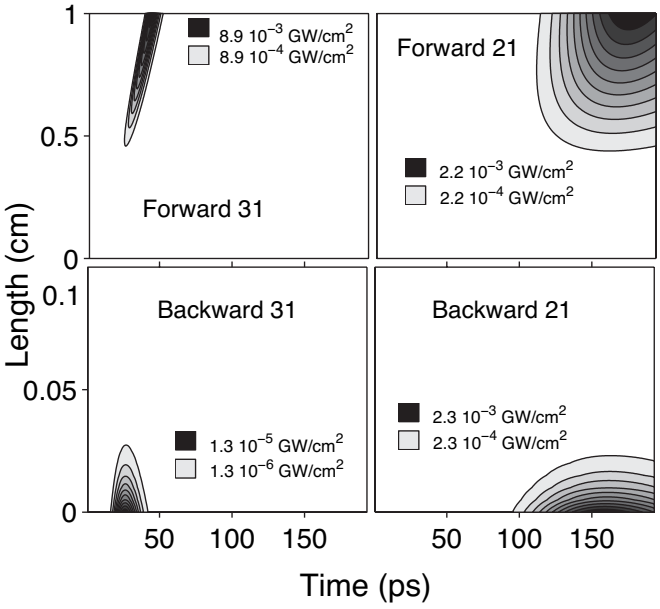

FIG. 14. Shapes of the ASE pulses for forward and backward ASE for $3\rightarrow1$ and $2\rightarrow1$ channels (solvent model). $I_p=I_0=222$ GW/cm^2. The case A: $d_{31}=d_{21}=7.73$ D.

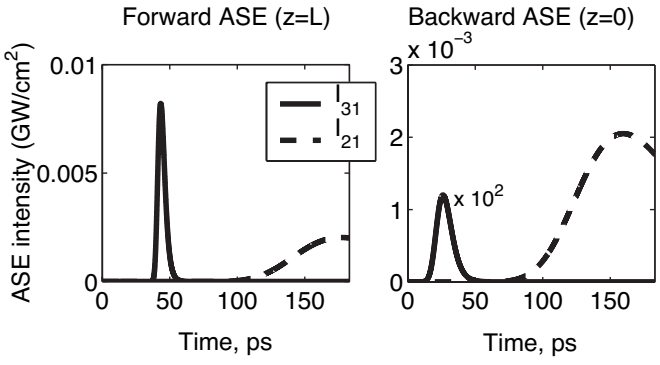

FIG. 15. Temporal shapes of the ASE pulses for forward and backward ASE for $3\rightarrow1$ and $2\rightarrow1$ channels (solvent model). Parameters are the same as in Fig. 14.

backward ASE spectra in the solvent model (Fig. 12) above the threshold pump level. To conclude, one can say that in the solvent model the threshold of backward ASE, $\gamma_{31}^{-}=\Gamma_{32}$, is shifted close to the threshold of the forward ASE, $\gamma_{31}^{+}=\Gamma_{32}$ [Eq. (16)]. Both forward and backward $2\rightarrow1$ ASE pulses experience a modulation similar to the molecular model (compare Figs. 10 and 16). The origin of these oscillations is found in the interaction of the forward and backward ASE pulses [27]. Indeed, the oscillatory pattern is absent when interaction of contrarily propagating ASE pulses is neglected.

1. Role of the ASE channel from pumped levels

In the simulations we ignore the $4\rightarrow1$ ASE channel from the pumped vibrational level. As mentioned in Secs. II B and III D, this ASE channel becomes important when the Franck-Condon factor of the $4\rightarrow1$ transition is large and the pump intensity exceeds the threshold ($I_p\gtrsim I_0'$), where the $4\rightarrow1$

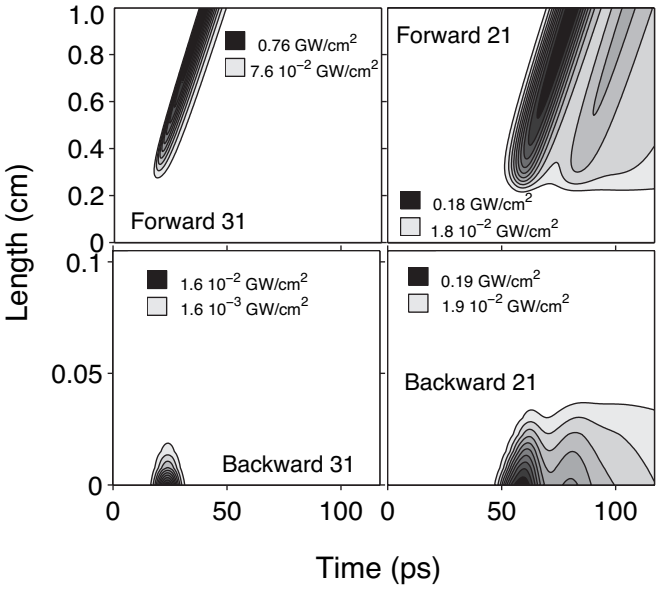

FIG. 16. Shapes of ASE pulses for forward and backward ASE for $3\rightarrow1$ and $2\rightarrow1$ channels (solvent model). $I_p=1.09I_0$, $I_0=271$ GW/cm^2. The case B: $d_{31}=6.18$ D, $d_{21}=7.73$ D.

threshold is defined by Eq. (17). Another reason for the suppression of the channel $4 \rightarrow 1$ is fast IVR depopulation of the level 4 (see Sec. III B). According to the molecular model [Fig. 6(a)], the threshold of the ASE transition $3 \rightarrow 1$ from the pumped level is $I_0 \approx 217$ GW/cm^2. This allows us to estimate the threshold of the same ASE channel $4 \rightarrow 1$ in the solvent model as 217 GW/cm^2. This value is very close to the threshold $3 \rightarrow 1$ channel 222 GW/cm^2 [Fig. 12(a)].

It is surprising that the threshold pump intensities of the $3 \rightarrow 1$ ($I_0 \approx 222$ GW/cm^2) and $4 \rightarrow 1$ ($I_0' \approx 217$ GW/cm^2) channels of forward ASE pulses in the solvent model are close to each other. Indeed, the first impression is that I_0 must be essentially smaller than I_0' because the relaxations rates $\Gamma_{32} = 1.99 \times 10^{10}$ s^{-1} and $\Gamma_{43} = 2.97 \times 10^{11}$ s^{-1} in Eqs. (16) and (17) differ by one order of magnitude. However, this is not the case for two reasons. One reason is the nonlinear (cubic) dependence of the pump rate on I_p [see Eq. (8)]. The other, more important, reason for this is the longer duration and, hence, smaller peak intensity of the $3 \rightarrow 1$ ASE pulse in the solvent model: Smaller peak intensities need higher pump levels to reach the threshold (16).

The discussed coincidence of I_0 and I_0' is absent for faster vibrational quenching, $\Gamma_{43}^{-1} < 3$ ps. Now the threshold pump level (17) of the $4 \rightarrow 1$ channel becomes higher than the $3 \rightarrow 1$ threshold. Thus, near the $3 \rightarrow 1$ threshold one can expect suppression of the ASE channel from the pumped level for subpicosecond vibrational quenching and $\tau_p = 100$ fs.

Thus, in the general case, the ASE spectrum in the solvent model consists of three components—41, 31, and 21. Clearly, the pulse 41 has the shortest duration. According to our simulations, the durations of the $4 \rightarrow 1$ and $3 \rightarrow 1$ forward ASE pulses near the threshold are about $\tau_{41} \approx 0.08$ ps and $\tau_{31} \approx 3$ ps, respectively. The experimental time resolution [13] is approximately $\tau_{\text{expt}} \approx 2$ ps. This implies a large experimental broadening of the short $4 \rightarrow 1$ pulse and, hence, strong suppression of the peak intensity of this ASE pulse: $I_{41}^{\max} \tau_{41} / \tau_{\text{expt}} \approx I_{41}^{\max} \times 0.04 \approx 0.01$ GW/cm^2. This value is close to the peak intensity of the $3 \rightarrow 1$ pulse near the threshold, $I_{31}^{\max} \approx 0.01$ GW/cm^2 (Fig. 15). It should be noted that the ratio of the intensities of the $4 \rightarrow 1$ and $3 \rightarrow 1$ channels depends strongly on the corresponding Franck-Condon factors which are chosen in our simulations to be rather close to each other. The ASE channel from the pumped level is suppressed if $\langle 4 | 1 \rangle \ll 1$.

2. Dynamical frequency shift

An important parameter of the solvent model [Fig. 2(b)] is the spacing between the lasing levels 3 and 2, $|\Delta\omega|$, caused by the dynamical relaxation of the excited solute molecule to a new equilibrium state with the solvent. Let us calculate $\Delta\omega$ for the PRL-L3 molecule (Fig. 3) in the DMSO solvent. To estimate the frequency shift due to the solvation ($\omega_{21} = \omega_{31} + \Delta\omega$), we use the reaction field theory formula [36] (in SI units)

$$\hbar \Delta\omega = \frac{1}{4\pi\varepsilon_0 a^3} \left[2\mathbf{d}_0 \cdot (\mathbf{d}_0 - \mathbf{d}_e) F(\epsilon, n) + (d_0^2 - d_e^2) \left(\frac{n^2 - 1}{n^2 + 2} \right) \right]. \tag{19}$$

Here, $\mathbf{d}_0$ and $\mathbf{d}_e$ are the permanent dipole moments of the solute molecule in the ground and excited states, respectively,

$$F(\epsilon, n) = \frac{\epsilon - 1}{\epsilon + 2} - \frac{n^2 - 1}{n^2 + 2} \tag{20}$$

is the reaction field factor; $4\pi\varepsilon_0 = 1.112\,65 \times 10^{-10}$ J^{-1} C^2 m^{-1}; ϵ and n are the static dielectric constant and the optical refractive index of the solvent, respectively; $\epsilon = 46.45$, $n = 1.478$, $F(\epsilon, n) = 0.66$ for dimethyl sulfoxide [36]. The radius of the spherical cavity of the solute $a \approx 8$ Å was computed as the sum of the radius of the PRL-L3 molecule (≈ 6.5 Å) and the van der Waals radius of the outermost chlorine atom (≈ 1.5 Å).

The permanent dipole moments of the PRL-L3 molecule (see Table II) were calculated making use of the DALTON code [37]. The permanent dipole moments of the first excited singlet state were calculated in the framework of the Hartree-Fock (HF) method by means of quadratic response (QR) formalism. The Sadlej basis set was employed to describe the iodine atom while for the other atoms we used the polarized split-valence 6-31G* basis set. Equation (19) results in the value for the shift $\Delta\omega \approx -379.7$ cm^{-1} or $\Delta\lambda \approx 13.5$ nm. This value is to be compared with the experimental value [13] $\Delta\lambda_{\text{expt}} \approx 20$ nm. The permanent dipole moments and, hence, the shift $\Delta\omega$ are sensitive to the computational method. For example similar calculations in the framework of the density functional theory (DFT) with the polarized split-valence basis set 6-311G* for the iodine atom give a smaller shift of $\Delta\lambda \approx 4$ nm. The difference between HF and DFT values of the ASE shift means that our simulations of $\Delta\lambda$ can be treated only as an estimate. To conclude, both molecular (Sec. II A) and solvent models give a spectral shift $\Delta\lambda$ of the same order of magnitude (~ 10 nm) as the experiment [13] (20 nm). Thus, the spectral shift does not allow us to select one of the discussed models.

V. CONCLUSIONS

Owing to the advancement in laser technology, many-photon-induced frequency-up-converted amplified stimulated emission has been observed and characterized in several recent well-recognized studies. The effect is associated with some outstanding features with rich physical content that pose a strong challenge to the theory of light-matter interaction. In an attempt to explain the given observations and to advance our understanding of the many-photon ASE process, a dynamical theory has been developed in the framework of two models described in this paper—called the molecular and solvent models. Special attention was paid to the spectral and temporal shapes of the co- and counterpropagating amplified stimulated emission pulses. The molecular model is based on two ASE channels: ASE transitions from the pumped vibrational levels and the decay transition from the

bottom of the excited-state potential well. The blueshifted ASE transition starts immediately from the pumped levels. The second ASE channel occurs from the bottom of the excited-state potential well, the population of which needs time for vibrational relaxation. Due to this circumstance, the second ASE channel is delayed. The spectral as well as the temporal shapes of backward and forward ASE pulses change drastically when the pump intensity crosses the threshold level, which is reached when the ASE rate of the first channel approaches the rate of nonradiative quenching of the pumped vibrational levels. This model explains the experimental observation of a blueshift of the forward ASE peak relative to the peak position of the backward ASE pulse that is nearly the same as the steady-state fluorescence. The outgoing ASE pulses leaving the cavity in the forward and backward directions have the same spectral features and consist of two components according to the two ASE channels. The ASE component corresponding to the blueshifted ASE channel is shorter than that corresponding to the redshifted ASE channel. This component is also shorter for the forward-propagating pulse than for the backward one. It is shown that the threshold value of the pump intensity for backward ASE pulses is essentially larger than for forward ASE.

The solvent model is more general and includes the extra ASE channel caused by the dynamical solute-solvent interaction. It accounts for the fact that the excited dye molecules instantaneously change their permanent dipole moment and that the relaxation of the solvent molecules around the newly formed dipole lowers the energy of the excited state. Usually, the time of such a relaxation is longer than the time of vibrational relaxation in the excited state. Radiative transitions from the bottom of this relaxed excited state result in an extra ASE channel, which is delayed and redshifted relative to the two "molecular" ASE channels. Contrary to the molecular model, the redshifted ASE pulse displays also a threshold behavior, with the threshold pump level slightly higher than for the molecular ASE channels. It is shown that the delay between the pulses and their duration depend on the pump level. All pulses experience shortening with the growth of the pump level. Our simulations display the modulation of the temporal shapes of the ASE pulses caused by the interaction between co- and counterpropagating ASE pulses. The experimental data available today do not allow us to unambiguously select one of the models. Time-resolved measurements are needed to make certain conclusions about the mechanism of the observed asymmetric behavior between the forward and backward ASE pulses. However, the solvent model is clearly preferable when the pump pulse is longer than the time of nonradiative depopulation of the pumped level. The field is certainly rich for further, combined, experimental and theoretical efforts to reach a basic understanding and to lay the groundwork for new applications in photonics.

ACKNOWLEDGMENTS

The authors are grateful to Professor Paras Prasad, ILPB, Buffalo, for useful discussion. This work was supported by the Swedish Research Council (V.R.) and by the STINT foundation. A.B. thanks the Swedish Research Council and the Swedish Foundation for International Cooperation in Research and Higher Education for financial support.

[1] G. S. He, J. D. Bhawalkar, C. F. Zhao, C.-K. Park, and P. N. Prasad, Opt. Lett. **20**, 2393 (1995).
[2] G. S. He, C. F. Zhao, J. D. Bhawalkar, and P. N. Prasad, Appl. Phys. Lett. **67**, 3703 (1995).
[3] G. S. He, L. Yuan, Y. Cui, M. Li, and P. N. Prasad, J. Appl. Phys. **81**, 2529 (1996).
[4] G. S. He, K.-S. Kim, L. Yuan, N. Cheng, and P. N. Prasad, Appl. Phys. Lett. **71**, 1619 (1997).
[5] A. Abbotto, L. Beverina, R. Bozio, S. Bradamante, C. Ferrante, G. A. Pagani, and R. Signorini, Adv. Mater. (Weinheim, Ger.) **12**, 1963 (2000).
[6] Y.-F. Zhou, F.-Q. Meng, X. Zhao, D. Xu, and M.-H. Jiang, J. Phys. Chem. Solids **62**, 1145 (2001).
[7] G. S. He, J. D. Bhawalkar, C. Zhao, C. K. Park, and P. N. Prasad, Appl. Phys. Lett. **68**, 3549 (1996).
[8] G. S. He, R. Signorini, and P. N. Prasad, IEEE J. Quantum Electron. **34**, 7 (1998).
[9] C. Ye, J. Wang, and D. Lo, Appl. Phys. B: Lasers Opt. **78**, 539 (2004).
[10] G. S. He, P. P. Markowicz, T.-C. Lin, and P. N. Prasad, Nature (London) **415**, 767 (2002).
[11] A. Baev, F. Gel'mukhanov, O. Rubio-Pons, P. Cronstrand, and H. Ågren, J. Opt. Soc. Am. B **21**, 384 (2004).
[12] A. Baev, V. Kimberg, S. Polyutov, F. Gel'mukhanov, and H. Ågren, J. Opt. Soc. Am. B **22**, 385 (2005).
[13] G. S. He, C. Lu, Q. Zheng, A. Baev, M. Samoc, and P. N. Prasad, Phys. Rev. A **73**, 033815 (2006).
[14] G. S. He, J. Dai, T.-C. Lin, P. P. Markowicz, and P. N. Prasad, Opt. Lett. **28**, 983 (2003).
[15] G. S. He, T.-C. Lin, S.-J. Chung, Q. Zheng, C. Lu, Y. Cui, and P. N. Prasad, J. Opt. Soc. Am. B **22**, 2219 (2005).
[16] P. P. Markowicz, G. S. He, and P. N. Prasad, Opt. Lett. **30**, 1369 (2005).
[17] G. S. He and P. N. Prasad, in *Nonlinear Optical Transmission and Multiphoton Processes in Organics*, edited by A. T. Yeates, K. D. Belfield, F. Kajzar, and C. M. Lawson, Proceedings of the SPIE Vol. 5211 (SPIE, Bellingham, WA, 2003), p. 1.
[18] S. Polyutov, I. Minkov, F. Gel'mukhanov, and H. Ågren, J. Phys. Chem. A **109**, 9507 (2005).
[19] D. J. Nesbitt and R. W. Field, J. Phys. Chem. **100**, 12735 (1996).
[20] S. Mukamel and R. Smalley, J. Chem. Phys. **73**, 4156 (1980).
[21] C. S. Parmenter, Faraday Discuss. Chem. Soc. **75**, 7 (1983).
[22] K. F. Freed and A. Nizan, J. Chem. Phys. **73**, 4765 (1980).
[23] I. Martini and G. V. Hartland, J. Phys. Chem. **100**, 19764

(1996).
[24] D. V. Shalashilin and M. S. Child, J. Chem. Phys. **119**, 1961 (2003).
[25] N. J. Turro, *Molecular Photochemistry* (W.A. Benjamin, New York, 1967).
[26] J. R. Lakowicz, *Principles of Fluorescent Spectroscopy* (Kluwer Academic/Plenum, New York, 1999), Chaps. 5 and 6.
[27] S. Polyutov, V. Kimberg, A. Baev, F. Gel'mukhanov, and H. Ågren, J. Phys. B **39**, 215 (2006).
[28] S. L. Schultz, J. Qian, and J. M. Jean, J. Phys. Chem. A **101**, 1000 (1997).
[29] T. Elsaesser and W. Kaiser, Annu. Rev. Phys. Chem. **42**, 83 (1991).
[30] H.-J. Hübner, M. Wörner, and W. Kaiser, Chem. Phys. Lett. **182**, 315 (1991).
[31] Q. Zhong, Z. Wang, Y. Sun, Q. Zhu, and F. Kong, Chem. Phys. Lett. **248**, 277 (1996).
[32] G. Angel, R. Gagel, and A. Laubereau, Chem. Phys. Lett. **156**, 169 (1989).
[33] A. Mokthari, J. Chesnoy, and A. Lauberau, Chem. Phys. Lett. **155**, 593 (1989).
[34] R. J. Sension, S. T. Repinec, A. Z. Szarka, and R. M. Hochstrasser, J. Chem. Phys. **98**, 6291 (1993).
[35] P. M. Felker, J. A. Syage, Wm. R. Lambert, and A. H. Zewail, Chem. Phys. Lett. **92**, 1 (1992).
[36] M. L. Horng, J. A. Gardecki, A. Papazyan, and J. Maroncelli J. Phys. Chem. **99**, 17311 (1995).
[37] T. Helgaker, H. J. Aa. Jensen, P. Jørgensen, J. Olsen, K. Ruud, H. Ågren, T. Andersen, K. L. Bak, V. Bakken, O. Christiansen, P. Dahle, E. K. Dalskov, T. Enevoldsen, H. Heiberg, H. Hettema, D. Jonsson, S. Kirpekar, R. Kobayashi, H. Koch, K. V. Mikkelsen, P. Norman, M. J. Packer, T. Saue, P. R. Taylor, and O. Vahtras, DALTON, ver. 1.0 (1997), http://www.kjemi.uio.no/software/dalton/dalton.html